ELSEVIER

Characterizing ramp events in floating offshore wind power through a fully coupled electrical-mechanical mathematical model

Lingte Chen [a], Jin Yang [a,*], Chengwei Lou [b]

[a] *James Watt School of Engineering, University of Glasgow, Glasgow, G12 8QQ, United Kingdom*
[b] *College of Information and Electrical Engineering, China Agricultural University, Beijing, 100083, China*

ABSTRACT

Floating Offshore Wind Turbines (FOWTs) exhibit a noteworthy nonlinear low-frequency dynamic response during rated and higher wind-wave scenarios, leading to a substantial exacerbation of its power characteristics, power stability, and wind energy forecast reliability. This study develops a fully coupled FOWT model to investigate the impact of wind and wave loads on wind power ramp events (WPREs), which integrates mechanical and electrical factors, including a spar buoy FOWT with generator, converter, and aero-hydro-servo-elastic (AHSE) dynamics. Results indicate that the floating structure enables periodic and significant WPREs of FOWTs, as wave load and platform natural motion causing low and ultra-low frequency response. In contrast to bottom-fixed offshore wind turbines (OWT), FOWTs exhibit a supplementary decline in rated power output ranging from 7.9 % to 40.5 % during WPREs. Moreover, ramp peak mainly depends on the aerodynamic loads, but become sensitive to wave loads characterized by wave heights over 2.52 m. FOWT power performance is highly unstable within the rated wind speed range, under WPREs within ultra short time period, resulting in failure to meet grid standards, emphasizing the external need for targeted power compensation and power signal processing. Overall, this study highlights the importance of pitch motion and wave load impact for WPRE study of FOWTs.

1. Introduction

In response to the challenge of global warming and climate change, there has been a significant surge in renewable energy production worldwide. Among these renewable options, wind energy stands out as one of the most efficient choices due to its widespread accessibility across the globe [1]. In addition, wind energy potential in deep water at offshore locations is up to 1.9 times that of onshore sites [2], leading to a notable increase in the deployment of offshore wind farms on available water bodies, particularly in nations with extensive deep coastlines. However, the increasing penetration of wind power poses significant challenges for grid operators in maintaining a safe, reliable, and cost-effective power system, owing to the uncertainty and variability associated with wind energy [3].

The abrupt power fluctuations, characterized by substantial magnitudes and brief durations, that manifest during the operation of wind turbines and wind farms are typically attributed to intricate physical processes and atmospheric phenomena, including thunderstorms, gusts, cyclones, and low-level jets [4]. These phenomena are collectively

referred to as Wind Power Ramp Events (WPREs). A key approach to address this challenge involves the quantification of WPREs, encompassing their intensity and frequency characteristics, as it aids in power system planning by providing crucial information for predicting necessary control measures [5]. In accordance with the findings of Reference [6], a power-ramp rate limit control was devised within the context of a wind-solar system. This control mechanism was designed to alleviate the impacts stemming from distinct fluctuations in power, specifically those attributable to wind, solar, and load dynamics of a substantial nature. Reference [7] studied the optimal daily peak-load scheduling for cascaded hydropower stations with consideration of wind energy uncertainty based on WPRE research. In a separate study [8], flexibility requirements based on WPRE analysis were employed to investigate cases involving energy storage and flexible power generation. Moreover, the accuracy of WPRE detection is pivotal in ensuring the reliability of wind power forecasting. Reference [9] introduced a range of data sampling techniques aimed at enhancing the accuracy of ramp alerts for wind power events by effectively addressing the issue of class imbalance. Reference [10] introduced pattern recognition to probabilistic

---

forecasting, leading to improved reliability and sensitivity of wind power predictions. Reference [11] improved prediction accuracy by employing precise wind process (WP) and wind process pattern (WPP) delineation in the pattern recognition stage. However, existing achievements have been primarily based on onshore or bottom-fixed Offshore Wind Turbine (OWT) types, leaving a research gap in WPRE studies related to Floating Offshore Wind Turbines (FOWT), as platform motions could result in elevated power output fluctuations and deteriorate the overall generating performance significantly [12].

Presently, only 3 grid-connected floating wind farms are in operation worldwide [13–15], making it challenging to directly reference and analyze open-access operational data. As an alternative approach, modifications could be made based on reliable mathematical models of wind turbines [16]. In the generic dynamic Wind Energy Conversion System (WECS) modeling developed by widely recognized International Electrotechnical Commission (IEC) and Western Electricity Coordinating Council (WECC) working groups, power characteristics are simplified and correlated with wind speed [17]. Such approaches, incorporating linearized aerodynamic models, consider the limited knowledge background of grid operators in dynamic analysis [18]. Despite the proven reliability of generic WECS models over the past decade [19–23], they cannot be directly applied as references for FOWT modeling, as they suffer from three crucial limitations:

(1) The simplified aerodynamic models fail to capture the significant variations in FOWT power characteristics [12,24].
(2) Research on FOWT power characteristics through FAST represented dynamic simulation codesare commonly based on the first-order induction generator provided by the code by default [25], while the research on synchronous generators with large inertia and low speed ratio is limited [26].
(3) The generic WECS models completely disregard the influence of wave loads on FOWT power, a factor that could potentially play a pivotal role in the emergence of WPREs [27,28].

Hence, there is a need for a comprehensive aero-hydro-servo-elastic (AHSE) dynamic model coupled with the WECS model. Therefore, in this paper, an interdisciplinary study is proposed to explore a mechanical-electrical fully coupled model to investigate real-world grid-connected scenarios involving WPRE cases. The graphic outline of the entire study is logically summarized in Fig. 1. Initially, a standard AHSE model was developed using the open-source FAST software, while a detailed high-order WECS model was created using Simulink. The dynamic analysis was performed using FAST, and the DLL (Dynamic Link Library) interface was employed to establish a connection between the WECS model and the generator, enabling the exchange of critical parameters such as electrical power and mechanical speed. This achieved a precise electromechanical coupling for the FOWT. Subsequently, adjustments were made to the hydrodynamically influenced FOWT equivalent power curve, accurately representing its electrical energy generation under real operational conditions. Optimized Swinging Door Algorithm (OpSDA) has conducted successful and impactful research in conventional wind farms by effectively combining "bumps" displaying diverse directional changes into neighboring slope segments, resulting in significant enhancement of detection precision [4], and is chosen to serve as a foundation for floating offshore WPRE data analysis. In this study, the OpSDA was tailored and optimized to suit the specific considerations of hydrodynamics, facilitating thorough data processing and analysis in the context of WPRE assessment.

The paper is organized as follows: Section 2 outlines the mathematical model formulation. Section 3 presents details of the flowchart-based simulation model setup based on Fig. 2. In Section 4, the relationship between hydrodynamic characteristics and power is examined under various wind and wave conditions, with detailed simulation results provided for a full range of conditions. Finally, Section 5 presents the conclusion.
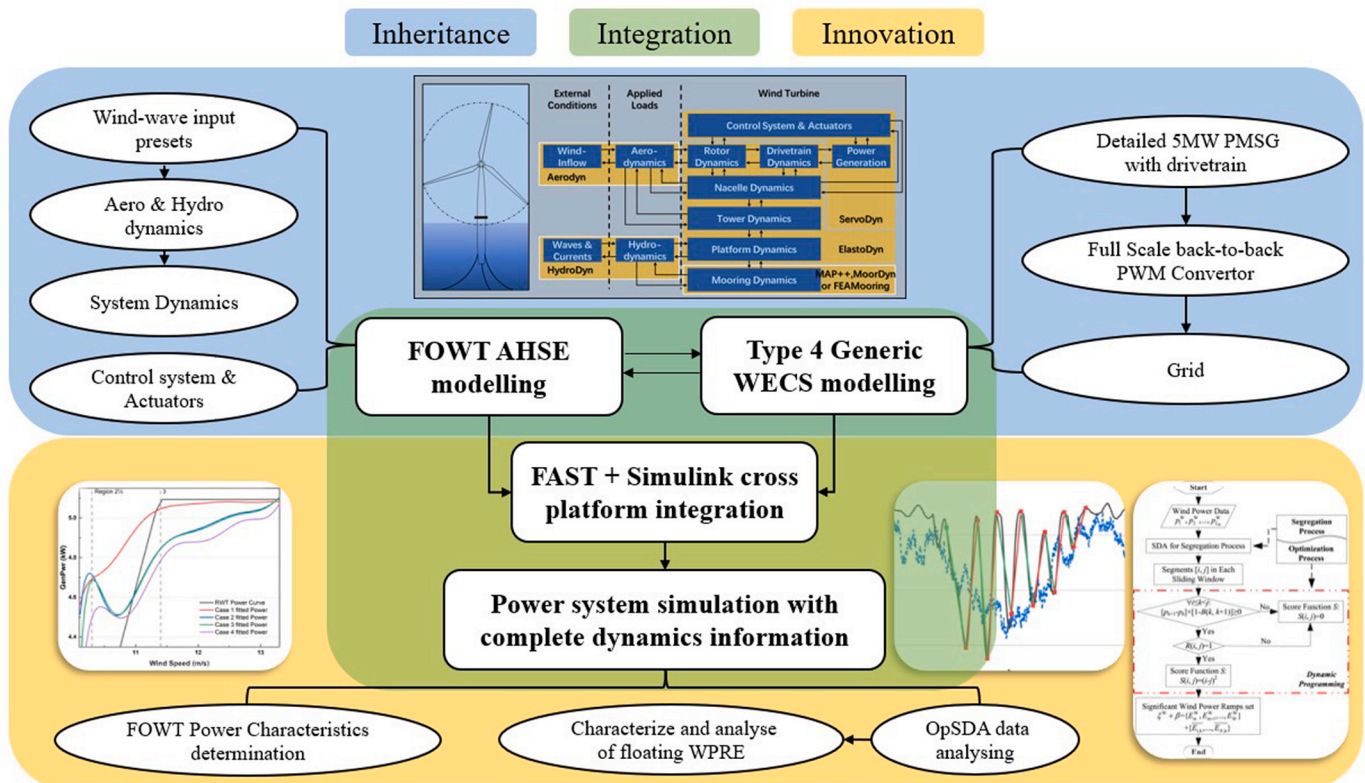

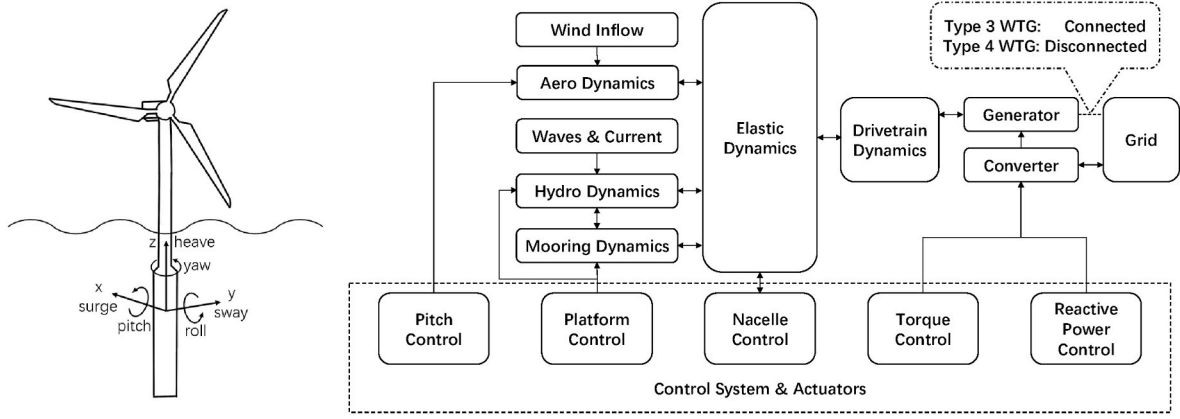**Fig. 1.** Graphic Outline of floating offshore WPRE research.

Fig. 2. Degrees of freedom and the block diagram for fully coupled FOWT model.

2. Complete system mathematical model formulation

The fully coupled model developed in this paper includes two distinct aspects of the complete system: modelling of the FOWT dynamics and that of the energy conversion system.

2.1. FOWT dynamic modeling

AHSE model is a mathematical model that describes the dynamic behavior of a FOWT in response to environmental loads, such as wind and waves. The model considers the interactions between the FOWT's structural, hydrodynamic, and aerodynamic components, as well as the control system used to stabilize the turbine in operation.

The FOWT model is used to predict the performance and stability of an FOWT under different operational conditions, such as different wind and wave conditions, which is used to design the control system for the FOWT. The model can also be used to optimize the design of the FOWT, such as selecting appropriate size, shape, and materials, to achieve required performance with reduced costs [29].

The FOWT model typically consists of several submodels, each representing a different aspect of the FOWT's behavior. The structural submodel represents the mechanical properties of the FOWT's structure, including its stiffness, mass, and damping. The hydrodynamic submodel represents the forces acting on the FOWT due to wave load, wave current, and added mass effects. The aerodynamic submodel represents the forces acting on the FOWT due to the motion of the air, including the lift and drag forces on the turbine blades. The control submodel represents the control system used to stabilize the FOWT, such as the mooring system or the blade pitch control. Thus, the model of the FOWT is shown in Fig. 2, which corresponds to the parameters of the AHSE dynamics and the complete WECS model.

The FOWT model is typically solved using computational methods, such as the finite element method or the boundary element method [30]. These methods allow the model to be solved quickly and accurately for a wide range of operational conditions, making it a valuable tool for the design and analysis of FOWTs.

2.2. WECS modeling

AHSE model of the FOWT can be established in detail through FAST, where it only uses a reduced order generator model to simulate the operating characteristics of the generator [31]. This simplified WECS model does not fully reflect the transient characteristics of the generation system. Therefore, this paper establishes a detailed permanent magnet synchronous generator (PMSG) system in MATLAB/Simulink through the interface of MATLAB/Simulink and FAST. This section will describe the modeling of the control strategy of PMSG and its back-to-back PWM converter.

2.2.1. Specification of the reference direction

Using the motor convention, looking towards the motor, the voltage and current will follow the cross-reference direction. The reference direction of the current and the reference direction of the magnetic flux produced by it follow a right-handed spiral relationship. The magnetic flux is in a right-handed spiral relationship with the induced electromotive force generated by itself.

2.2.2. Generator voltage equation and flux equation

When the positive directions of the stator, rotor voltage and current adopt the motor convention, the voltage equation and flux linkage equation of the PMSG in the rotating synchronous coordinate system are (1) and (2), respectively

$$v_s = R_s i_s + \frac{d(L_s i_s)}{dt} + \frac{d}{dt}\left(\Psi_f e^{j\theta_e}\right) \tag{1}$$

$$\begin{cases} \Psi_d = L_d i_d + \Psi_f \\ \Psi_q = L_q i_q \end{cases} \tag{2}$$

where v_s is the stator terminal voltage vector of the generator, R_s is the resistance of the stator winding of the generator, i_s is the stator current vector, L_s is the stator inductance, θ_e is the electrical angle rotated by the rotor, and Ψ_f is the flux linkage obtained by the interlinkage between the magnetic field generated by the permanent magnet and the stator winding. L_d and L_q are the self-inductances in the stator d-q axis, as shown in (3).

$$\begin{cases} L_d = L_{dm} + L_{\sigma s} \\ L_q = L_{qm} + L_{\sigma s} \end{cases} \tag{3}$$

where L_{dm}, L_{qm} are the excitation inductance of the stator d-q axis, respectively. $L_{\sigma s}$ is the leakage inductance of the stator phase winding.

In the synchronous rotation coordinate system, the positive direction of the d-axis is the positive direction of the direct axis of the rotor magnetic pole, and the positive direction of the q-axis is the direction ahead of the d-axis by 90° of electrical angle. The d-q axis rotates with the rotation of the rotor magnetic poles, then in the *dq* coordinate system, the stator voltage equations can be expressed as:

$$v_d = R_s i_d + L_d \frac{di_d}{dt} + \frac{d\Psi_f}{dt} - \omega_e L_q i_q \tag{4}$$

$$v_q = R_s i_q + L_q \frac{di_q}{dt} + \omega_e\left(L_d i_q + \Psi_f\right) \tag{5}$$

where v_d, v_q are the d-q axis components of the PMSG stator terminal voltage; i_d, i_q are the d-q axis components of the stator current, respectively.

2.2.3. Generator torque equation

The electrical torque of the generator T_e depends on its flux linkage Ψ_s and current vector i_s, which is illustrated in the following equations:

$$T_e = \frac{3}{2} n_p \Psi_s \times i_s \tag{6}$$

$$\Psi_s = \Psi_d + j\Psi_q \tag{7}$$

$$i_s = i_d + j i_q \tag{8}$$

where n_p is the generator pole pair number. Thus generator T_e can be further derived by (2), (7), and (8).

$$T_e = \frac{3}{2} n_p \left(\Psi_f i_q + \left(L_d - L_q \right) i_d i_q \right) \tag{9}$$

Equation (9) reflects that T_e is related to both the d and q axis currents. However, if $L_d = L_q$, or $i_d = 0$;

$$T_e = \frac{3}{2} n_p \Psi_f i_q \tag{10}$$

Therefore, to control the electrical torque of the PMSG, its q-axis current i_q should be controlled. As for the approach to meet the prerequisites of (10), since the Interior Permanent Magnet Synchronous Generator (IPMSG) does not satisfy $L_d = L_q$, a current closed-loop control is usually used to make the current command $i_d = 0$ to control the electrical torque T_e.

2.2.4. Rotor-side converter control strategy

The control block diagram of the d-q axis current of the rotor-side converter is shown in Fig. 3.

As aforementioned, after the d-axis is oriented to the rotor magnetic pole, if the d-axis current i_d can be controlled to be 0, then the electrical torque T_e of PMSG is proportional to the q-axis current i_q. By controlling i_q, T_e can be effectively controlled [26].

$$i_q^* = -\frac{2 T_e^*}{3 p_p} \tag{11}$$

The reference value i_q^* is calculated as (11), where n_p is the number of pole pairs of PMSG rotor. T_e^* is the reference value of electrical torque

that is determined by the principle of maximum power tracking (MPPT).

According to the MPPT with the optimal power characteristic, as long as the electrical torque of the generator T_e is controlled in real time according to the speed of the rotor ω_{wt}, the relationship between these two parameters can fit the optimal torque curve to achieve MPPT [32]. The MPPT control principle is explained by (12) and (13).

$$P_{mech\_opt} = \frac{3}{2} \rho C_{p\_max} \pi R^2 \left(\frac{R\omega_{wt}}{\lambda_{opt}} \right) \approx K_{opt} \omega_{wt}^3 = P_e^* \tag{12}$$

$$T_{mech\_opt} = \frac{P_{mech\_opt}}{\omega_{wt}} \approx K_{opt} \omega_{wt}^2 = T_e^* \tag{13}$$

where ρ is the air density, R is the rotor radius, K_{opt} is a constant which can be calculated from (12) by keeping both tip speed ratio and wind turbine airfoils constant and equal to their optimal values λ_{opt} and C_{p_max}.

To sum up, the control strategy on the generator side is that the outer loop adopts active power closed-loop regulation, and the deviation between the actual power P_e fed back by the grid and the reference power P_e^* is adjusted by PI controller and used as the reference value i_q^* of the generator's current. The q-axis current i_q can in turn adjust the electromagnetic torque of the generator and then adjust the output power to achieve maximum power tracking [33].

2.2.5. Grid-side converter control strategy

The operating target of the grid-side converter is to transmit the power generated by the PMSG to the grid with high quality. This means that the waveform of the grid-connected current is sinusoidal, and in phase with the grid voltage, that is, the ideal power factor equals 1.

The dynamic equation of grid-side converter simplified model is:

$$v_{gsc} - u_g = L \frac{di}{dt} \tag{14}$$

where u_g is the instantaneous value of the grid voltage; v_{gsc} is the output voltage of the grid side converter, which is a pulse waveform of equal amplitude and unequal width, that is, a PWM (pulse width modulation) wave. It can be decomposed into the fundamental component and a series of harmonic voltage components, where the fundamental current
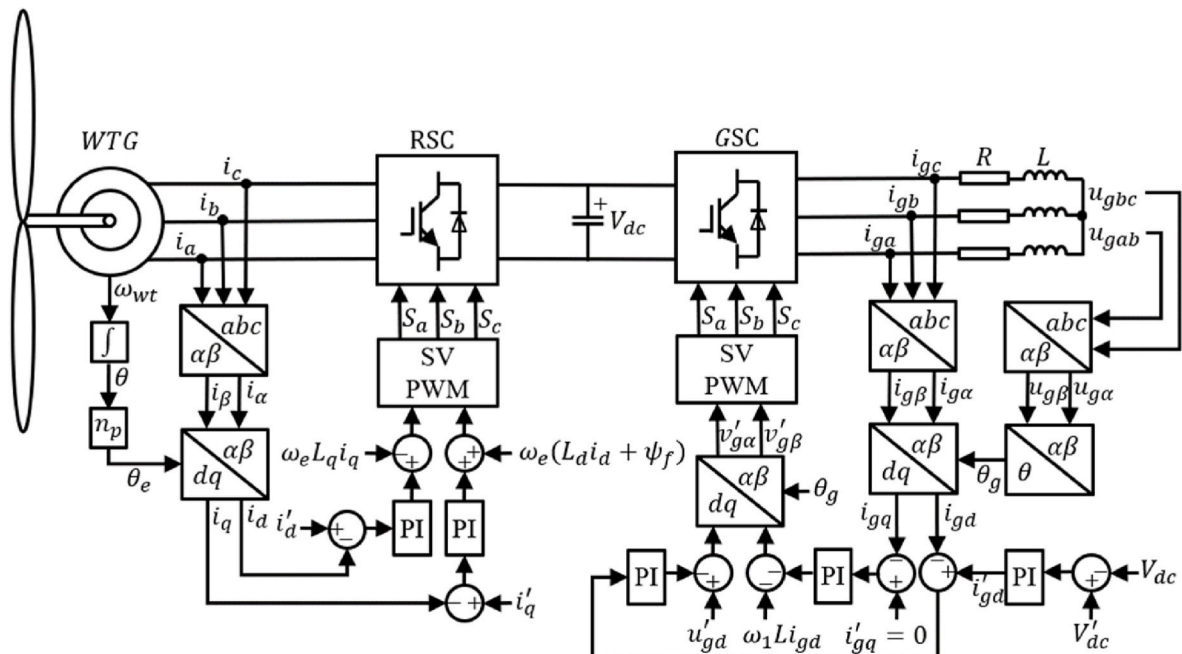

Fig. 3. Type 4 WTG full scale PWM converter control diagram.

is the main object of attention.

Since the set target power factor is 1, then $u_{gq} = 0$. Orienting the d-axis in the synchronous rotating coordinate system of the grid voltage, it is:

$$\begin{cases} u_{gd} = Ri_{gd} + L\dfrac{di_{gd}}{dt} - \omega_g Li_{gq} + v_{gd} \\ 0 = Ri_{gq} + L\dfrac{di_{gq}}{dt}\omega_g Li_{gd} + v_{gq} \\ C\dfrac{dV_{dc}}{dt} = S_d i_{gd} + S_q i_{gq} - i_{load} \end{cases} \tag{15}$$

where ω_g is the grid frequency in rad/s. Using parameters in the dq coordinate system, the active power P_g and reactive power Q_g output by the grid-side converter can be obtained as below.

$$P_g = u_{gd}i_{gd} + u_{gq}i_{gq} = Ui_{gd} \tag{16}$$

$$Q_g = -u_{gd}i_{gq} = -Ui_{gq} \tag{17}$$

Therefore, concluding from (16) and (17), by controlling the dq axis current, the active and reactive power that the converter absorbs or supplies from the grid can be controlled separately. Moreover, active power and reactive power do not affect each other, i.e. realizing decoupling control. The control block diagram of the grid-side converter is also shown in Fig. 3.

3. Model Test Set-up

The floating platform is referred as the OC3 Hywind spar buoy whereas the wind turbine model used is an NREL 5 MW wind turbine [34]. Table A and Table B show the detailed parameters of the platform with mooring system, and the wind turbine, respectively.

In this study, FAST v8 [31] is used to predict the performance and stability of an FOWT under different operational scenarios, such as different wind and wave conditions, and to design the control system for the FOWT. The model can also be used to optimize the design of the FOWT, determining details such as its size, shape, and materials, to improve performance and reduce costs. FAST v8 uses a modular approach, allowing users to choose the appropriate level of details for each submodel based on specific needs of their analysis. The tool also includes a range of options for inputting environmental loads and turbine parameters, making it a versatile tool for simulating the performance of FOWTs under a wide range of operational conditions [35]. With dedicated communication port with Simulink, the mechanical dynamics model based on FAST can be coupled with the high-order WECS model used in this study to conduct more comprehensive and detailed experimental research on the electrical performance analysis of the complete system.

3.1. Case study settings

The coupled model simulates in a variable step solver with a total calculation time of 3600s in each case. In Simulink, the time step for the WECS model is set to $2 \times 10^{-6}s$, whereas in FAST, the time step for the AHSE model is reduced to $2 \times 10^{-3}s$ to minimize deviations from the electrical module. In addition, the time step of the meshing and numerical calculations performed by the Hydrodyn module also needs to be adjusted to $2 \times 10^{-3}s$ to match the AHSE model settings. Various responses were analyzed for translational (i.e. surge, sway, heave) and rotational (i.e. pitch, roll, yaw) motions along the x, y, and z axes. The motion of one of the floating platforms in six degrees of freedom is shown in Fig. 1. Specific environmental conditions are set as follows.

(a) Case 1: Bottom-fixed OWT at 12 m/s wind speed
(b) Case 2: FOWT at 12 m/s wind speed with no wave
(c) Case 3: FOWT at 12 m/s wind speed with normal regular wave

(d) Case 4: FOWT at 12 m/s wind speed with huge irregular wave
(e) Case 5: FOWT at wind-wave conditions within all operational range.

It is worth noting that Cases 1 to 4 are differentiated settings to explore the influence of hydrodynamics on FOWT power characteristics, but the requirements of the control variable method are still followed for comparison between every two adjacent cases. As for Case 5, FOWT undertakes testing on wind and wave conditions within its operational range in order to investigate the patterns and interrelationships between varying wind and wave conditions and the quality of power output. The tested input wind speed ranges from 8 m/s to 14.8 m/s with an interval of 0.2 m/s. The wave conditions considered are irregular and with ranges in height from 0m to 6.1m within 10-year return period sea state based on western Taiwan offshore location. [36]. Table 1 shows listed case details. It is important to emphasize that wave conditions vary significantly in different maritime regions. To study more severe wave conditions than those in Taiwan Strait, reference can be made to the environments in areas represented by the Ireland offshore [37] and the North Sea [38].

3.2. Developed wind-wave scenarios

In this study, a turbulent wind field was created using TurbSim v1.5 [39] and inflow vertically into swept area of the wind turbine. The field has a height of 155m and a width of 145m, consisting of 225 grid points with 15 points along both the vertical and horizontal axes. The center of the field coincides with the hub point of the turbine. The turbulence intensity adheres to the specifications outlined in category-C of IEC 61400–1 [40]. Moreover, the wind speed fluctuations, as depicted in the Velocity Spectra of various wind models based on the Turbsim-generated data, exhibit minimal high-frequency variations, with the peak in the spectra occurring near zero frequency. This indicates a general stability in wind speed, characterized by slower fluctuations compared to the higher and more concentrated distribution of hydrodynamic natural frequencies observed in the OC3-Hywind FOWT, reinforcing that the majority of detected WPREs with durations less than 15s primarily originate from hydrodynamic influences, such as waves or natural frequency responses.

The FAST input files specify the ocean wave setting for this study, which involves analyzing and comparing regular and irregular waves.

Table 1
Case setting details.

Case	Turbine type	Input wind (m/s)	Input wave			Scenario
			Model	H_s (m)	T_p (s)	(western Taiwan offshore based)
1	OC3-Tripod	12.0	–	0	0	Bottom-fixed OWT reference
2	OC3-Hywind	12.0	–	0	0	Still water conditions
3	OC3-Hywind	12.0	Regular	1.67	5.17	Normal sea conditions
4	OC3-Hywind	12.0	Irregular	5.5	9.4	Northeast monsoon sea conditions
5	OC3-Hywind	8.0–14.8	Irregular	0~6.1	0~10.2	Sub-10-year return period conditions

10-year return period wave reference at western Taiwan offshore: $H_s = 6.1m$, $T_p = 10.4s$.
50-year return period wave reference at western Taiwan offshore: $H_s = 9.1m$, $T_p = 13.0s$.

To simulate the actual irregular waves, JONSWAP spectral model [41] is selected in Hydrodyn with peak enhancement factor $\gamma = 2.08$ specialized for Taiwan Strait environment [36]. The relationship between significant wave height H_s and average zero up-crossing period T_z is determined by local wind generated wave equations (18) and (19) in duration limited offshore condition [42].

$$H_s = 0.0146 \times D^{5/7} U^{9/7} \tag{18}$$

$$T_z = 0.419 \times D^{3/7} U^{4/7} \tag{19}$$

$$T_p = 1.28 \, T_z \tag{20}$$

where T_p is peak wave period, U is wind speed in m/s at $10m$ above mean sea level, and D is duration in hours. Relationship between T_p and T_z for waves based on the JONSWAP spectrum can be expressed as (20) [43]. Therefore, it is possible to consolidate (18) to (20) to derive the relationship between H_s and T_p.

$$T_p = \left(3.510 \times D^{1/9}\right) \times H_s^{4/9} \tag{21}$$

Based on (21), the wave characteristics for different durations are compared with the 4 representative conditions (illustrated in Table 1) of the western Taiwan offshore [36] as shown in Fig. 4(a), with the curve for a 12-h duration ($D = 12$) selected as wave setting reference for H_s and T_p in Case 5.

3.3. WPRE definition and detection

Research focused on WPREs can be categorized into three primary domains: WPRE detection, WPRE prediction, and WPRE application. The initial phase, WPRE detection, involves extracting wind power slopes from real or forecasted wind power data through mathematical algorithms and definitions of wind power ramps. The accuracy of WPRE prediction is significantly reliant on the precision of WPRE detection.

An influential solution in this domain is the OpSDA, which was initially introduced in 2016 [44]. OpSDA has gained prominence within the WPRE detection field and has been adopted as a data preprocessing technique in various studies to enhance wind power prediction accuracy [4,10,11,45,46]. A key aspect highlighted in Ref. [44] underscores the significance of mitigating "fake ramp events" to enhance the effectiveness and precision of WPRE detection when utilizing OpSDA. However,

in normal environmental conditions containing small wave loads, these "fake ramp events" characteristics could potentially disrupt WPRE detection. Consequently, the calibration of parameters such as the sampling interval and casement door width becomes pivotal. In the debugging process of this study, the pivotal calibration of parameters, including time resolution and threshold width, resulted in a substantial improvement in detection success as the model iteratively converged towards optimal settings. Differing from Ref. [4], OpSDA data processing was executed twice on time-domain power data: first with small time resolution (0.05s) and threshold width (0.1) for merging adjacent ramps, and then with larger settings (1s time resolution and 0.3 threshold width) to minimize errors stemming from abrupt slope changes.

In the following Sections, the power curve of the simulation outcome will be analyzed, revealing several significant WPRE cases beyond 20 % of the total FOWT capacity. This observation was made despite the wind speed being set close to the rated value and the sea wave setting being normal. The possible observed fluctuation is of considerable concern as it approaches the limits set by major countries and regions that utilize large-scale offshore wind resource, for meeting operational requirements. Table 2 summarizes the WPRE boundary definitions of well-known reference [4], for wind farms comprising OWTs, with additional requirements from independent system operators (ISOs) available in Ref. [47].

4. Results and discussion

In this section, the verification of the PMSG and its converter model in MATLAB/Simulink is performed based on the power curve outlined in the existing literature for a 5 MW reference offshore wind turbine [34]. Subsequently, an assessment of the corresponding dynamic motion of the FOWT and the fluctuation in output power is conducted, taking into account the predetermined conditions of Cases 1–4. The power quality of the prevailing wind and wave circumstances is also analyzed and compared. Finally, this section discusses the improved power curves and operating criteria for FOWTs. It is noteworthy that the simulation time resolution is 0.002 s, and the power output is recorded for a representative 1-h period of wind and wave conditions corresponding to the set cases.
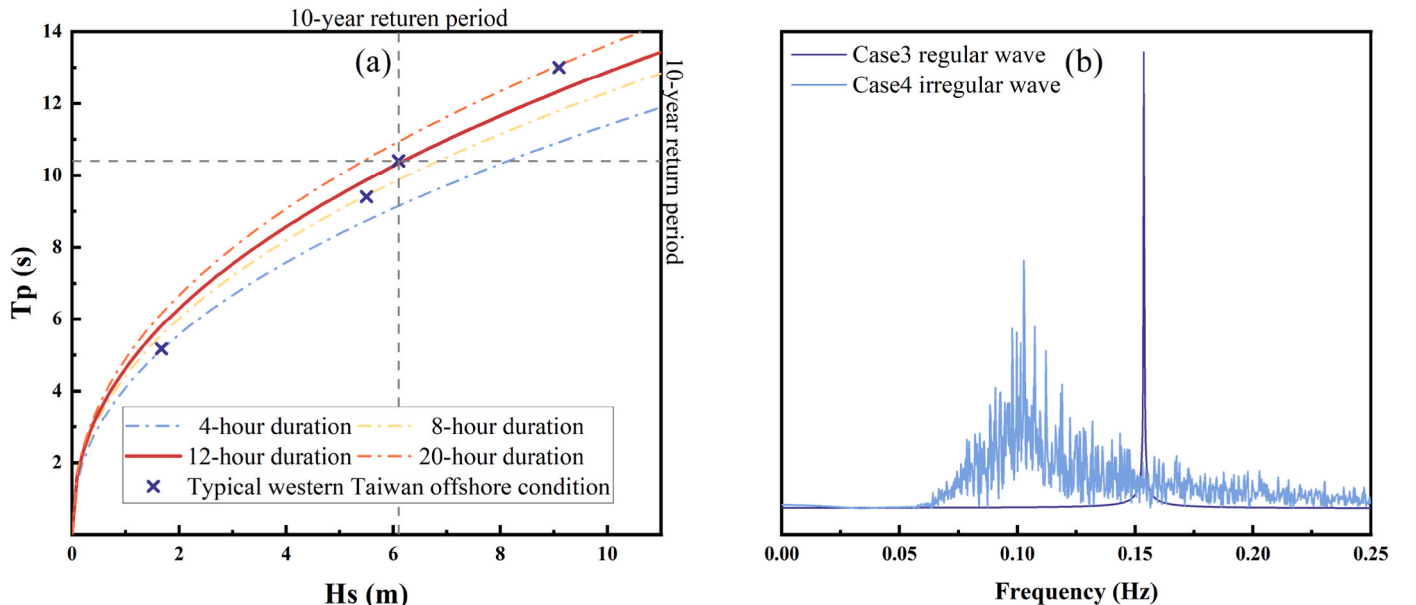

Fig. 4. Input wave (a) characteristic determination, and (b) spectral analysis of Case 3 and Case 4.

Table 2
WPRE definitions of OWTs.

Organization	Frequency Stability Focus			Unit Commitment (UC) Focus	
	Within 2s	Within 5s	Within 60s	Within 4h	∞
Eltra	$\Delta P / P_{nom} \leq 20\%$				
SvK		$\Delta P / P_{nom} \leq 20\%$			
E.ON			$\Delta P / P_{nom} \leq 10\%$		
Scotland			$\Delta P / P_{nom} \leq 20\%$		
Def 1					$\Delta P / P_{nom} \leq 20\%$
Def 2				$\Delta P / P_{nom} \leq 20\%$	
Def 3					$\dfrac{d\left(\Delta P / P_{nom}\right)}{dt} \leq 3\%$

ΔP: difference between the maximum and minimum power during the specified time period.
P_{nom}: rated output power of the WECS.
Unit of Def 3 is p.u./min, ramp duration without limitation is symbolled as ∞.

4.1. Validation of coupled models and WPRE detection methodology

To assess the accuracy of the WECS model, the dynamics were evaluated utilizing the OC3-Tripod bottom fixed OWT model [48]. Multiple sets of power and mechanical torque data were examined in the absence of ocean waves, and with a steady-state wind input. The findings of the experiments exhibited a remarkable level of agreement with the established 5 MW baseline wind turbine model [34], indicating a high degree of consistency. This outcome is illustrated in Fig. 5(a), which further substantiates the validity and reliability of the generator and converter models. This alignment substantiates the efficacy and accuracy of the proposed model in simulating the behavior and performance of the aforementioned reference wind turbine., and there is a consistent coherence between the generator power and output power. Moreover, during the WECS model's commissioning process, careful attention was given to monitor and authenticate the intermediate variables through diligent efforts. As a result, it was proved that these intermediate variables exhibit a high degree of reliability and accuracy, affirming their credibility in the overall system.

The modified OpSDA's detection performance, as illustrated in Fig. 5

(b), is evaluated against power output data at 0.05s time resolution. The performance diagram employed aligns with the design in Ref. [4], offering a visual comparison. The x-axis represents the ratio of "Start-YES" to "Start-YES-End-YES," while the y-axis reflects the proportion of "End-YES" within "Start-YES-End-YES." Results approaching the upper-right corner signify a superior Critical Success Index (CSI) and heightened WPRE detection accuracy. In contrast to the [4] result at 1-min time resolution (indicated as "Ref" in Fig. 5(b)), all cases in this study exhibit improved detection accuracy, affirming OpSDA's suitability for floating WPRE detection, especially evident in 1-min time resolution cases due to the brief duration of a single WPRE cycle. Notably, FOWT based Case 2 outperforms OWT based Case 1, attributed to the platform's natural motion enhancing slope characteristics. Conversely, Cases 3 and 4, incorporating wave loads, exhibit reduced detection accuracy, with larger waves yielding better CSI. Case 3 presents a particularly formidable challenge due to subtle parameter deviations leading to the splitting of significant WPREs into smaller slopes, ultimately resulting in detection failures.
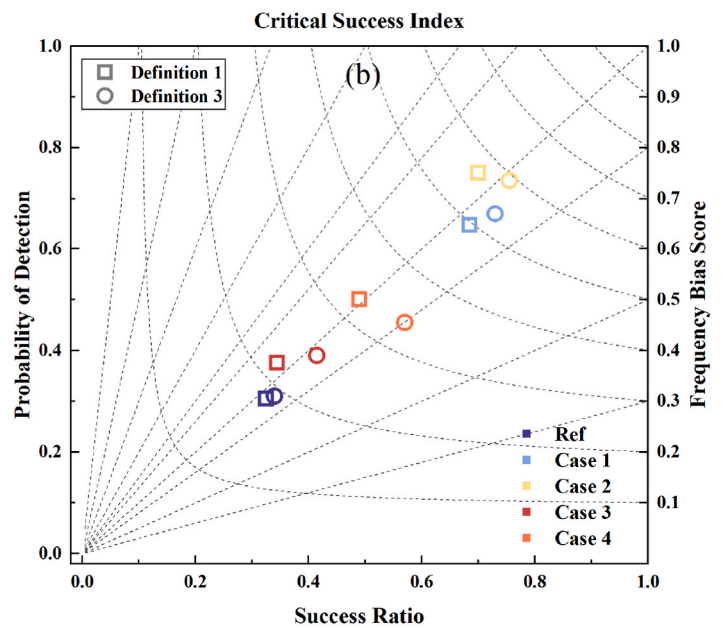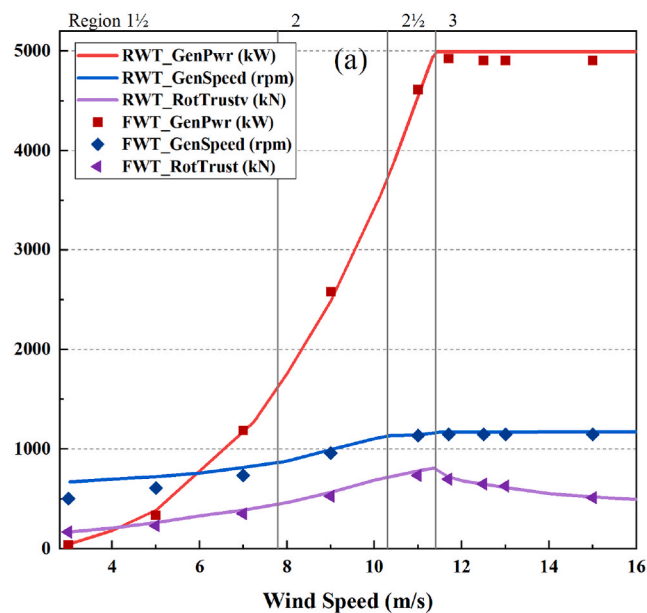
Fig. 5. Validation outcome of (a) power and torque characteristic of the proposed fully coupled model and the reference model, and (b) revised OpSDA detection performance under definition 1,3 compared to Ref. [4] at 1-min time resolution.

4.2. Impact of hydrodynamics on power characteristics

In Fig. 6, the temporal segments of simulation results showcase four distinct learning cases within the coupled model's comprehensive dynamics. This temporal domain exhibits a phase characterized by conspicuous wind speed stall, accompanied by a coherent power ramp evident in the conventional bottom-fixed OWT denoted as Case 1. In contrast, despite the absence of wave-induced forces, the FOWT in study Case 2 induces oscillations in the platform's natural frequency due to rapid wind speed variations, exacerbating the amplitude of the power ramp. Cases 3 and 4, which incorporate wave loading, moderately amplify the overall slope's magnitude relative to Case 2. Notably, under the influence of substantial wave loading as depicted in Case 4, a significant high-frequency WPRE is detected. Conversely, the wave scenario reflecting the rated operational state in Case 3 effectively fragments the complete WPRE into multiple segments, thereby impacting the accuracy of WPRE detection.

In order to further link the relationship between the power characteristics and the hydrodynamic characteristics, it is necessary to do a qualitative analysis of the Degree of Freedoms (DoFs) motion of the floating platform. Fig. 7 depicts the mean value and range of translational and rotational dynamics during simulation period for the Cases 1–4 scenarios. Relatively speaking, in Case 1, the bottom-fixed OWT exhibits negligible motion across 6 DoFs. Conversely, the FOWT in Cases 2 through 4 demonstrates a discernible range of motion across all DoFs. By comparing Cases 2 and 3, it becomes evident that the resulting motions in each DoF are highly similar. This finding suggests that the aerodynamics of the FOWT largely govern its overall dynamics, with hydrodynamics playing a minimal role, under common wind-wave conditions. When comparing the common waves in Case 3 with the 10-year sea state waves set in Case 4, it is observed that the latter case emerges a lower average angle and better stability within the surge motion, which is often attributed to the presence of irregular waves.

Despite there being no notable differences in the mean value when comparing the remaining 5 DoFs, there is an increase in the fluctuation range of 0.5m in heave and 0.7° in pitch.

The spectrum of the active power in the low frequency range for Cases 1 to 4 is depicted in Fig. 8. The most intuitive conclusion is that FOWT has a significant difference in pitch and surge motion compared with fixed OWT. Analysis of the frequency spectrum for Case 1 indicates that, with the exception of the DC component located around the origin, the low-frequency components of the power output can be attributed solely to the dynamic characteristics of the FOWT introduced by the floating platform. The comparison between Case 1 and Case 2 provides insight into the impact of ocean waves on the dynamics of floating platforms. In the absence of waves, the pitch and surge motion of FOWT had a decisive impact on the output power fluctuation, causing the spectrum's peak frequency to coincide with the FOWT natural frequency below 0.05 Hz. Comparing Case 2 to Case 3–4, it further demonstrates that wave activity on the platform induces additional power fluctuations, with the resulting harmonic frequency corresponding to the oscillation period of the waves. These findings suggest that ocean waves play a significant role in influencing the power output of floating platforms, emphasizing the additional requirement for structural vibration mitigation approaches, such as the integration of wave energy conversion systems [49] and turned mass dampers [50]. A comparison between Case 3 and Case 4 reveals that larger waves lead to a decrease in the peak frequency of the platform's motion component, resulting in a larger platform motion period. Moreover, it can be observed that the periodic waves introduced in Case 3 possess a relatively concentrated and robust weight, while the irregular P-M wave body introduced in Case 4 exhibits a low but decentralized weight within a specific frequency bandwidth.

This study also focuses on the power characteristics of FOWT on account of its inherent structural vibration. Curve fitting for the power characteristic is based on the wind speed and output power data, excluding the initial 600 s of the startup phase, and encompassing the
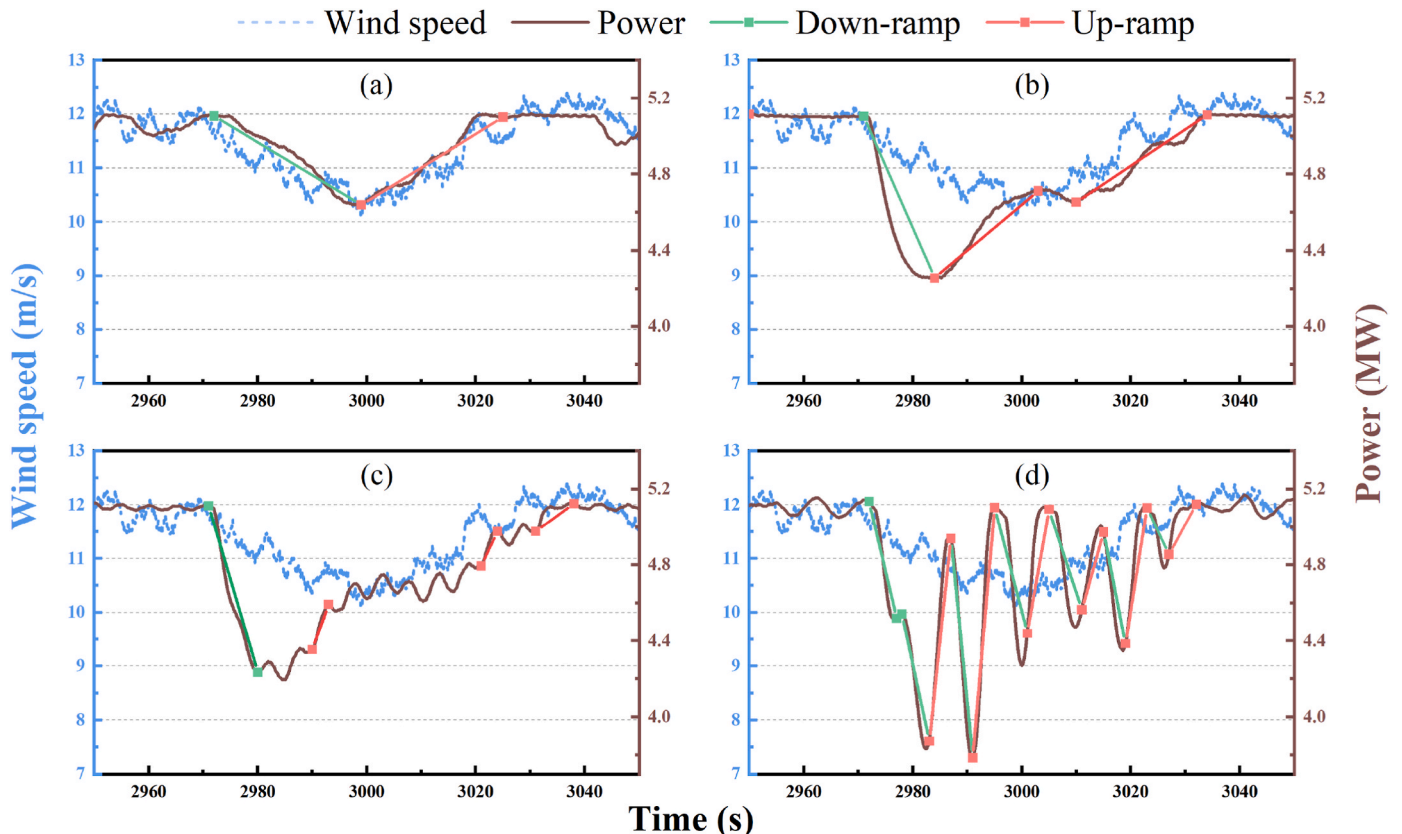

Fig. 6. Segments of simulation results for (a) Case1, (b) Case2, (c) Case3, (d) Case4, including wind speed, WECS output power, major WPRE components.
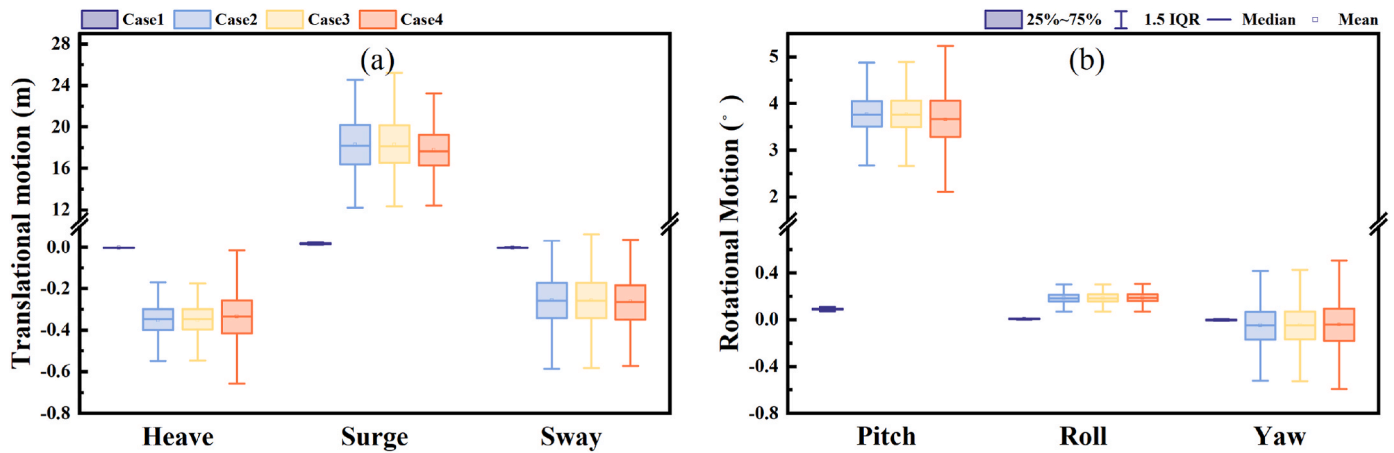
Fig. 7. Statistics of wind turbine (a) translational, (b) rotational motions under Case 1 to 4.
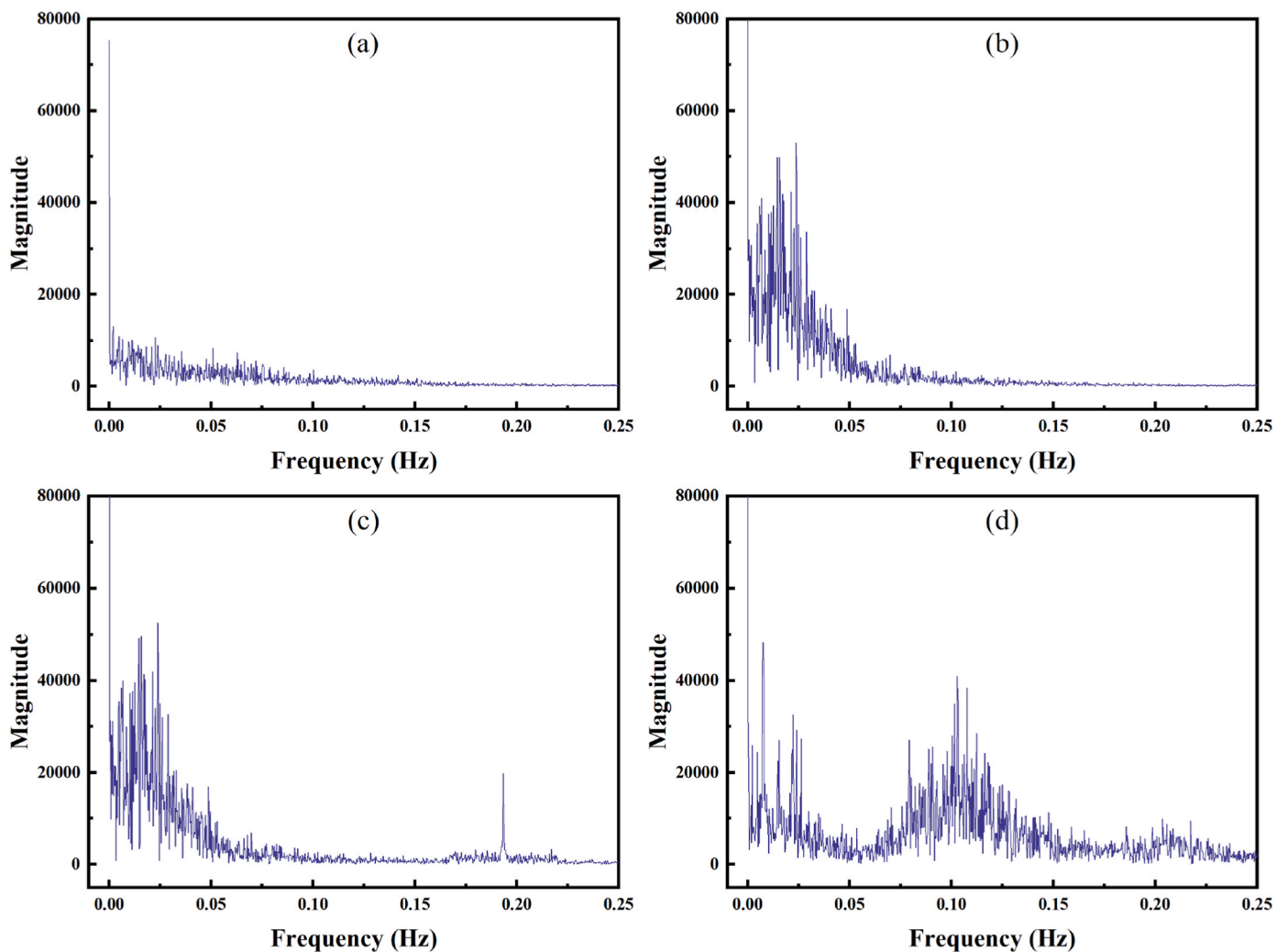

Fig. 8. Spectral analysis of FOWT output power in (a) Case1, (b) Case2, (c) Case3 and (d) Case4.

remaining 3000 s of simulation duration. The fitted curve in Fig. 9 illustrates the overall relationship between wind speed and power. However, the presence of data points significantly deviating from the fitted curve highlights the impact of hydrodynamics on the correlation between wind speed and power, which the curve cannot fully capture. The analysis indicates that, as the wave conditions intensify in the

examined scenario, the relationship between wind speed and power deviates from the expected ideal power characteristic. Instead, it becomes more focused and confined within a considerably lower power range. Despite the wind speed being set at 12 m/s for all four cases, turbulent wind conditions resulted in wind speed fluctuations ranging from 10 to 14 m/s. The trend observed in the 4 cases at low wind speed is
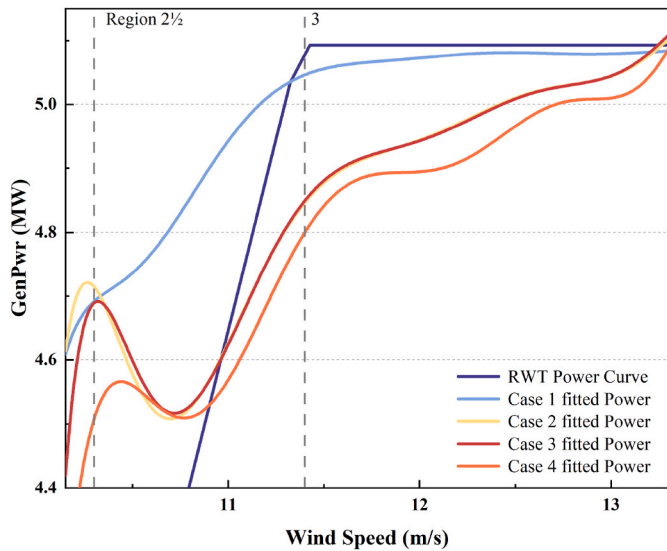
Fig. 9. Fitted power characteristics of FOWT in Cases 1–4 wind & wave conditions.

consistent with the operational behavior of conventional wind turbines, demonstrating a positive correlation between wind speed and power output below the rated wind speed. Notably, the power characteristic curve of the fixed foundation Case 1 did not match previous validation test results, particularly with respect to high power output at low wind speeds. This phenomenon is likely attributable to the rotor's limited responsiveness, characterized by its significant inertia, which impedes swift adjustments to abrupt variations in wind speed. The large inertia associated with the PMSG employed in this experiment may result in the rotor not promptly reaching its target speed during episodes of rapid wind speed reduction, contributing to the observed deviations in the power curve, particularly in the lower wind speed range. This underscores the influence of the rotor's inertia on the dynamic response of the wind turbine system. Cases 2–4 showed significant dynamic impacts, resulting in power fluctuations of up to 20 % of the rated power in extreme situations. Furthermore, these impacts became more severe with increasing wave intensities.

Fig. 10 is the density estimation of wind speed and FOWT output power. As the hydrodynamic influence gradually increases, a comparison of the 4 cases reveals that the center of FOWT output power
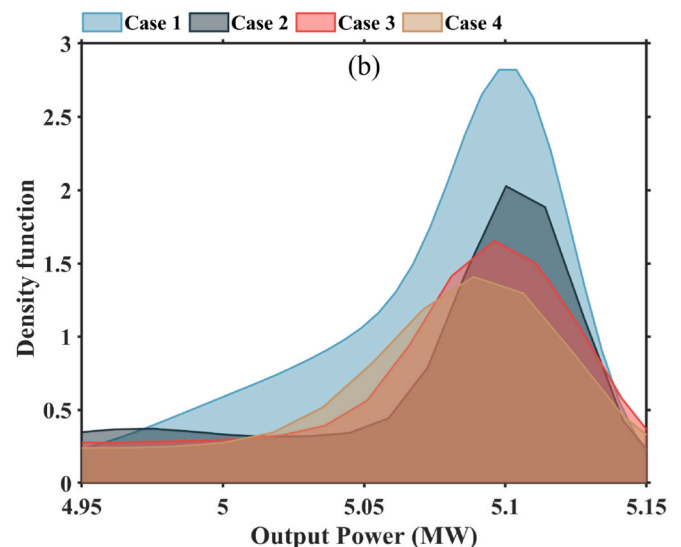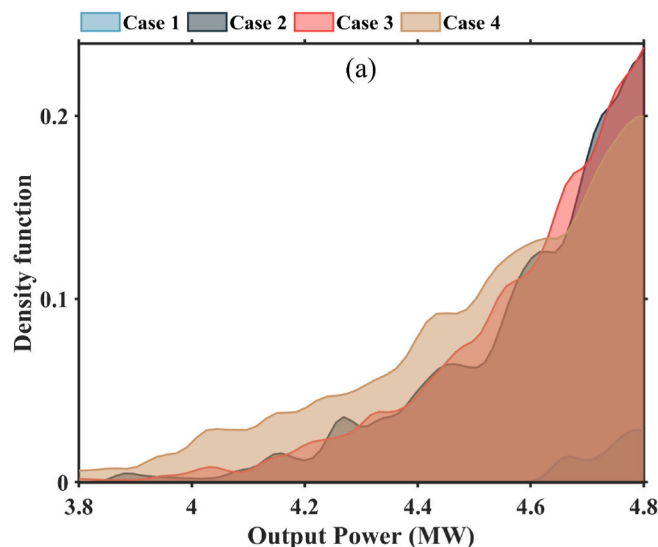
distribution thus drops, and the occurrence of extreme scenario samples below 90 % of the rated power increases. Cases 2 and 3 exhibit a similar trend within the power drop range, suggesting that the primary determinant of the significant power drop is the movement of the floating platform influenced by the wind. In contrast, the impact of regular sea waves appears to be minimal.

4.3. WPRE analysis of FOWT

The processed results of time-domain power output from the four different learning cases are analyzed using the OpSDA, leading to the presentation of the statistical distribution of power ramps in Fig. 11. This representation effectively reveals several significant observations. Firstly, the alteration rate of WPREs for the FOWT, operating without the influence of sea wave load, mirrors that of the bottom-fixed OWT upon comparison between Case 1 and Case 2. Secondly, with increasing wave load, a steeper incline becomes apparent and accelerates progressively. Lastly, the analysis of power fluctuations demonstrates a consistent tendency, wherein the rate of increase in power during upward transitions exceeds that during downward transitions in Case 3 and Case 4.

Fig. 12 presents a comparative analysis of the significant WPREs observed in bottom fixed OWT (OC3-Tripod) and FOWT (OC3-Hywind) during a simulation period of 3600s characterized by intense wave activity. To facilitate a clear comparison, H_s and T_p were aligned with 10-year condition of western Taiwan offshore. The power fluctuation observed in fixed foundation OWTs is generally restricted, with peak values being recorded around the rated wind speed. Nevertheless, the power fluctuation per minute for a single OWT occasionally surpasses the standard during wind speeds ranging from 9.4 m/s to 11.4 m/s. On the other hand, FOWTs display a substantially higher power fluctuation in the complete wind speed spectrum when compared to the reference OWTs. The active power fluctuation of FOWTs, subject to severe waves, is challenging to be constrained within the required range, with the peak value occurring when the wind speed is 9.8 m/s.

As shown in Fig. 13, the present study examines the maximum power fluctuation within time period of 2s, 5s, and 60s under varying wind-wave conditions. The findings demonstrate that the most severe power fluctuations occur at high wind speeds and large waves of 9.6 m/s. With decreasing wave heights, the wind speed corresponding to the maximum power fluctuation gradually increases and approaches the rated value of 11.4 m/s. The outcomes of the analysis reveal that the difference in power fluctuations for the same wave at different wind speeds is limited
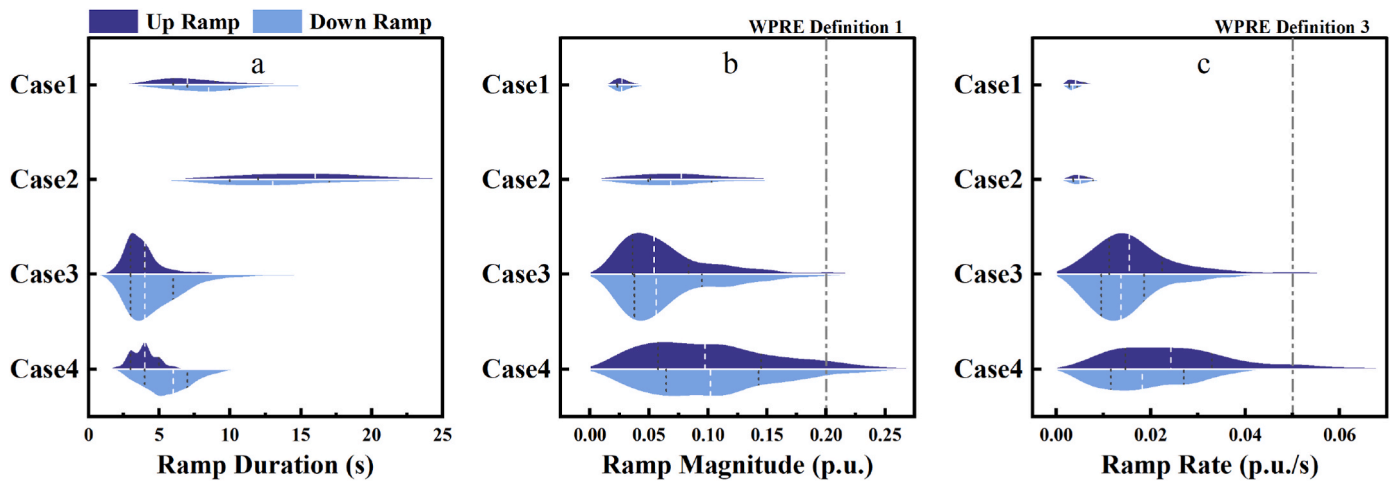

Fig. 10. Kernel density estimate (bandwidth = 0.02) of FOWT output power at (a) WPRE range, (b) rated range.

Fig. 11. Probability distribution for the study cases of (a) the WPRE duration, (b) the WPRE Magnitude, (c) the WPRE rate.
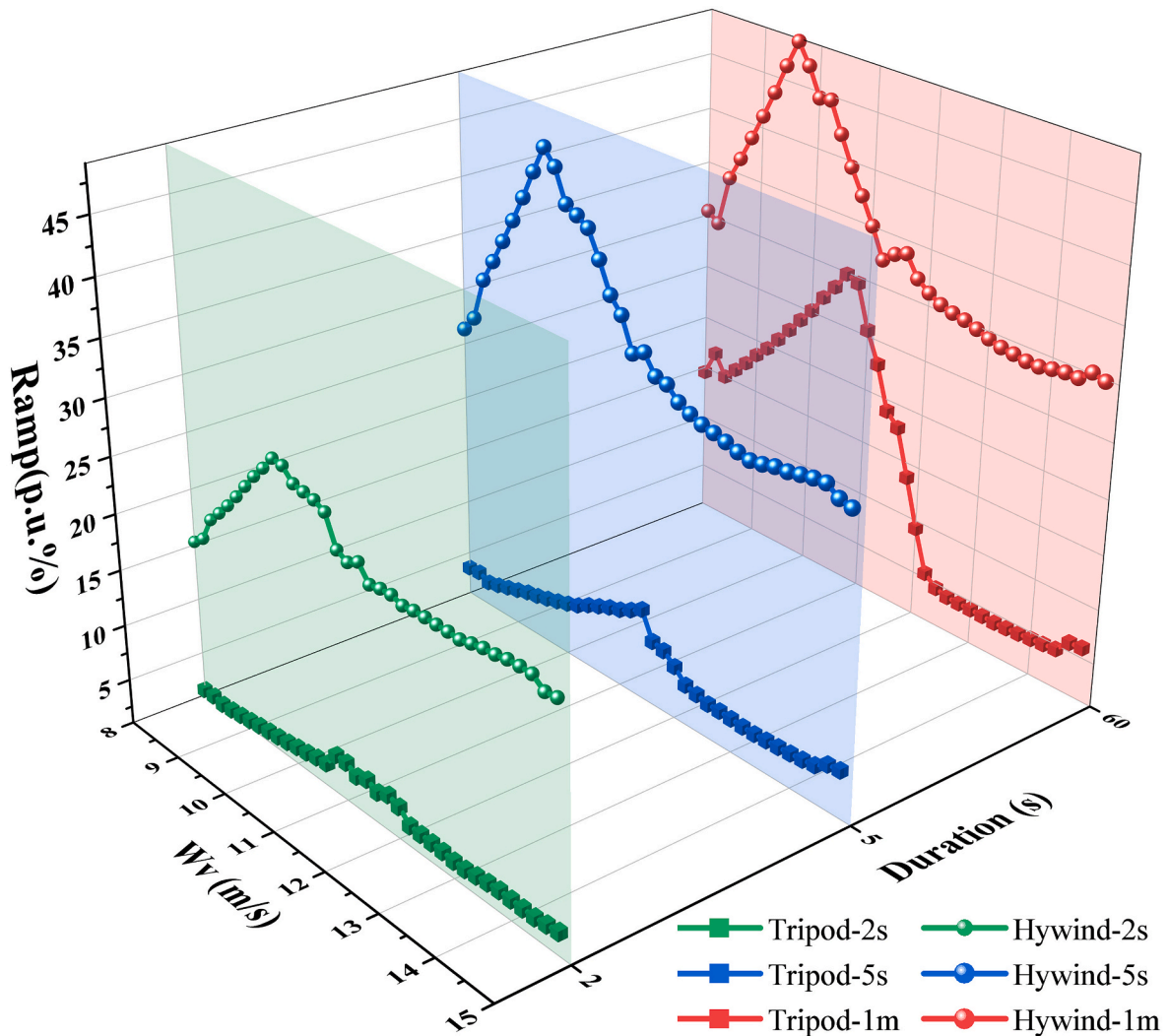

Fig. 12. Significant WPRE magnitude comparison between bottom-fixed OWT and FOWT under 10-year return period wave conditions at western Taiwan offshore.

over a short time period, indicating that the second-level instantaneous power fluctuation primarily reflects the impact of ocean waves. Additionally, it is observed that the second-level power fluctuation remains below the threshold of 20 % as long as the H_s does not exceed 3.27m,

across all wind speeds. However, in contrast to (a) and (b), the power fluctuation in (c) is generally unsatisfactory under most wind-wave conditions, with a "dead zone" observed at wind speeds between 10.4m/s-11.8 m/s as shown in Fig. 13, where all sea wave conditions

(a) Significant WPRE magnitude within 2s (%)

(b) Significant WPRE magnitude within 5s (%)

(c) Significant WPRE magnitude within 60s (%)

(d) Significant WPRE magnitude without time resolution (%)
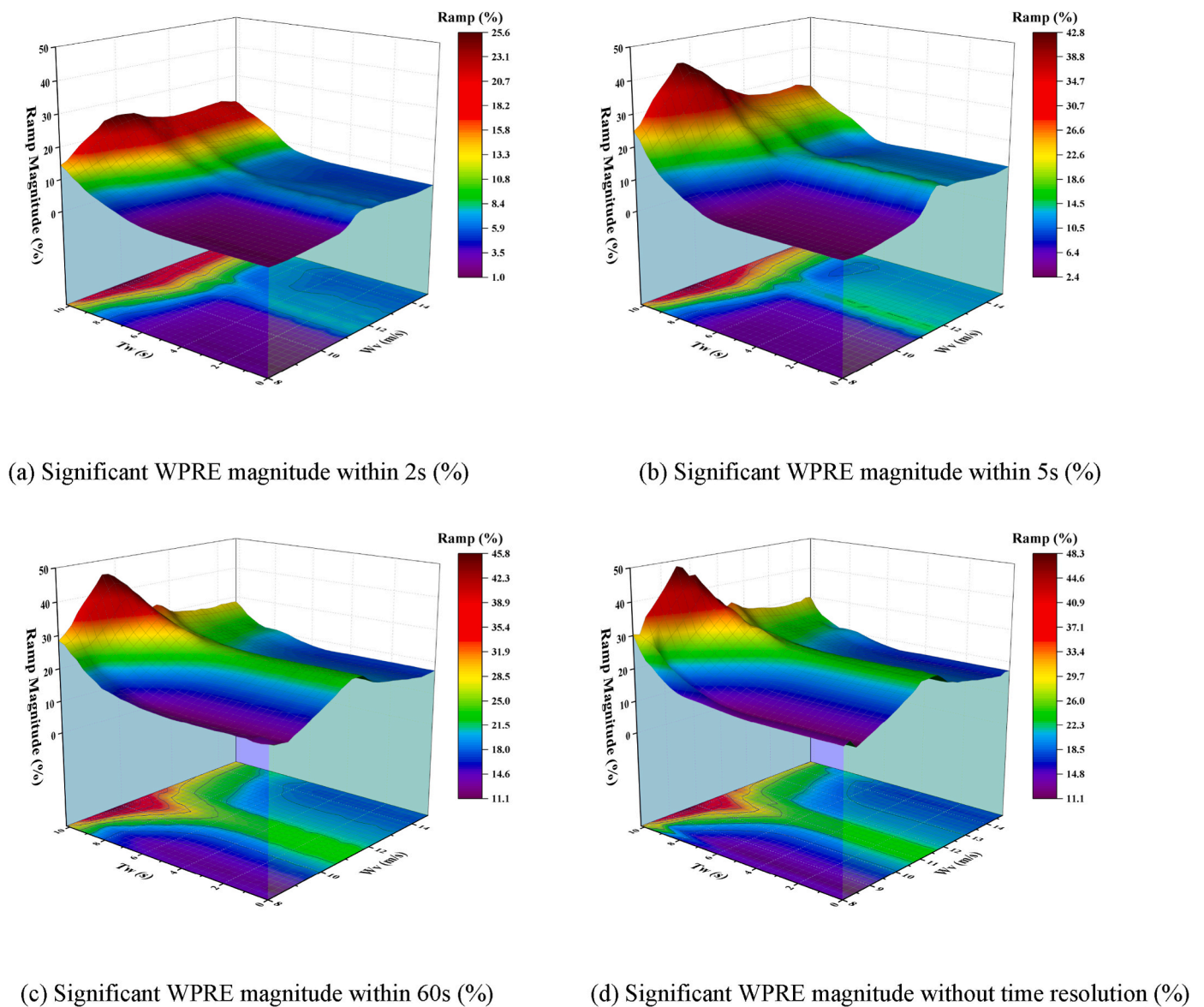
Fig. 13. Maximum WPRE magnitude under operational wind and wave range at different time spans in Case 5.

cannot limit the fluctuation within 20 % of the rated power. Nonetheless, based on the overall test results, the wind-wave boundary for FOWTs to operate compliantly has been identified. This finding can be utilized as a reference for future research aimed at quantifying the level of power quality enhancement in combination with existing research on dynamic optimization and power compensation using power conditioning equipment.

By analyzing the most significant WPRE cases withindifferent time spans (2s, 5s, 60s and ∞) from Fig. 14, it can be observed that there is an intersection between the analyzed data and the fully-developed wind-wave scenario (blue straight line) [51]. The analysis reveals that the wind speed corresponding to the maximum fluctuation point is approximately 11 m/s, and T_p is around 6.6s. It is noteworthy that the wind speed associated with the maximum fluctuation point is in close proximity to the rated wind speed of 5 MW wind turbine (11.4 m/s), indicating that such wind-wave conditions are likely to occur frequently during the designed operational range of FOWT.

5. Conclusion

In summary, this study developed an integrated, fully coupled

mathematical model for FOWTs, delving extensively into the interactions between wind-induced and wave-induced loads and their resultant influence on WPREs. By synergizing mechanical and electrical constituents within a complete framework encompassing a spar buoy FOWT equipped with generator, converter, and AHSE dynamics, the following conclusions are drawn:

1. **Manifestation of Periodic WPREs through Floating Dynamics:** The distinctive buoyant configuration of FOWTs engenders a cyclic recurrence of WPREs characterized by their periodic and pronounced dynamics. This phenomenon arises from the interplay between wave-induced loads and platform oscillations, giving rise to low (0.1–0.5 Hz) and ultra-low frequency (less than 0.05 Hz) responses. In contrast to conventional bottom-fixed offshore counterparts, FOWTs exhibit amplified power fluctuations during WPREs, thus highlighting the unique dynamical traits inherent to these floating structures.

2. **Ramp Peaks and Load Dynamics Relationship:** The zenith of ramping phenomena primarily hinges on aerodynamic loading dynamics, albeit exhibiting heightened sensitivity to wave-induced loading effects, particularly discernible when significant wave
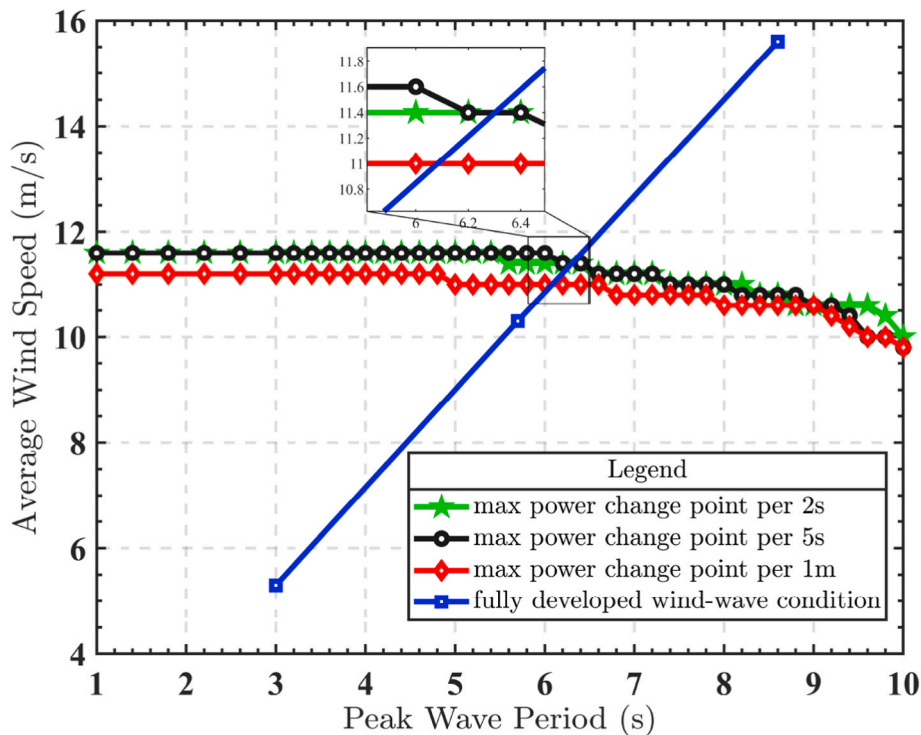
Fig. 14. The coordinates of the most significant wind power ramp events and fully developed wind-wave relationship.

heights surpass the threshold of 2.52 m. This underscores the pertinence of accounting for wave-induced loading intricacies in the design, operation, and risk management of FOWTs.

3. **Operational Impact of Peak WPREs under Rated Wind and Wave Conditions:** Notably, the pinnacle of WPREs surfaces conspicuously within the ambit of rated wind and wave conditions. This convergence heralds a distinctive operational scenario wherein the turbine perpetually operates within the ambit of the most exacerbated WPRE manifestations. This operational facet underscores the turbine's perpetual exposure to the most adverse ramping dynamics, accentuating the intricacies of power instability inherent within this specific operational regime.

4. Significance of pitch motion and wave-induced loading

The significance of pitch motion and the profound ramifications of wave-induced loads in shaping the landscape of WPREs for FOWTs are unequivocally underscored. These dynamics constitute pivotal parameters for explicating the transient response of FOWTs across diverse operational scenarios.

In summary, this study not only addresses a significant research gap pertaining to WPRE studies in the domain of FOWTs, but also engenders profound insights into the underpinning dynamical intricacies shaping the operational integrity and reliability of wind energy systems. Pioneering the integration of hydrodynamic complexities and mechanical motion dynamics within a holistic model framework, this investigation advances the strategic design, deployment, and grid integration of FOWTs.

CRediT authorship contribution statement

Lingte Chen: Conceptualization, Methodology, Simulation, Writing – original draft. **Jin Yang:** Supervision, Validation, Writing – review & editing. **Chengwei Lou:** Writing – review & editing.

Declaration of competing interest

The authors declare that they have no known competing financial interests or personal relationships that could have appeared to influence the work reported in this paper.

Appendix

A
Key Properties of the modified NREL 5-MW Floating Platform

Property	Value
Blades & Hub (kg)	109931
Nacelle (kg)	247291
Tower (kg)	287128
Platform roll & pitch inertia (kg.m2)	6.31×10^9

B
Key Properties for the modified NREL 5-MW Baseline Wind Turbine

Property	Value
Wind Turbine Parameters	
Rating capacity of power	$5 MW$
Rotor orientation, Configuration	$Upwind, 3\ Blades$
Control type	$Variable\ Speed,$
	$Collective\ pitch$
Rated wind speed	$11.4\ m/s$
Rated rotor speed	$12.1 rpm\ (1.267 rad/s)$
Pitch angle initialization	0°
Gearbox ratio	$1 (\text{direct drive})$
Drivetrain efficiency	97%
Generator Parameters	
Nominal Power	$5.297 MW$
Nominal Torque	$4.18 MN \bullet m$
Number of pole pairs	100
Stator resistance	0.08Ω
D-axis Inductance	$8.38 mH$
Q-axis Inductance	$8.38 mH$
Flux linkage established by magnets	$17.8 V \bullet S$
Grid Side Parameters	
Grid Side Resistance	0.08Ω
Grid Side Inductance	$4 mH$
DC Reference Voltage	$6400 V$
DC capacitor	$4 \mu F$
Grid Parameters	
Grid Voltage	$4 kV$
Grid Frequency	$50 Hz$

References

[1] IEA, Renewables 2019 – Market Analysis and Forecast from 2019 to 2024, 2019.

[2] W. Musial, D. Heimiller, P. Beiter, G. Scott, C. Draxl, Offshore Wind Energy Resource Assessment for the United States, No. September, 2016, 2016.

[3] M. Lochmann, H. Kalesse-Los, M. Schäfer, I. Heinrich, R. Leinweber, Analysing wind power ramp events and improving very short-term wind power predictions by including wind speed observations, Wind Energy 26 (6) (2023) 573–588, https://doi.org/10.1002/we.2816.

[4] M. Cui, J. Zhang, C. Feng, A.R. Florita, Y. Sun, B.M. Hodge, Characterizing and analyzing ramping events in wind power, solar power, load, and netload, Renew. Energy 111 (Oct. 2017) 227–244, https://doi.org/10.1016/J.RENENE.2017.04.005.

[5] J. Hu, L. Zhang, J. Tang, Z. Liu, A novel transformer ordinal regression network with label diversity for wind power ramp events forecasting, Energy 280 (Oct. 2023), 128075, https://doi.org/10.1016/J.ENERGY.2023.128075.

[6] S. Das, B. Singh, Mitigating impact of high power ramp rates in utility grid integrated wind-solar system using an RLMAT adaptive control strategy, IEEE Trans. Energy Convers. 38 (1) (2023) 343–354, https://doi.org/10.1109/TEC.2022.3192994.

[7] X. Jin, et al., Wasserstein metric-based two-stage distributionally robust optimization model for optimal daily peak shaving dispatch of cascade hydroplants under renewable energy uncertainties, Energy 260 (Dec. 2022), 125107, https://doi.org/10.1016/J.ENERGY.2022.125107.

[8] X. Fang, Q. Hu, R. Bo, F. Li, Redesigning capacity market to include flexibility via ramp constraints in high-renewable penetrated system, Int. J. Electr. Power Energy Syst. 128 (Jun. 2021) 106677, https://doi.org/10.1016/J.IJEPES.2020.106677.

[9] Y. Fujimoto, Y. Takahashi, Y. Hayashi, Alerting to rare large-scale ramp events in wind power generation, IEEE Trans. Sustain. Energy 10 (1) (2019) 55–65, https://doi.org/10.1109/TSTE.2018.2822807.

[10] H. Fan, et al., Fluctuation pattern recognition based ultra-short-term wind power probabilistic forecasting method, Energy 266 (2023), 126420, https://doi.org/10.1016/J.ENERGY.2022.126420. Mar.

[11] F. Wang, et al., Wind process pattern forecasting based ultra-short-term wind speed hybrid prediction, Energy 255 (Sep. 2022), 124509, https://doi.org/10.1016/J.ENERGY.2022.124509.

[12] T. Wakui, M. Yoshimura, R. Yokoyama, Multiple-feedback control of power output and platform pitching motion for a floating offshore wind turbine-generator system, Energy 141 (2017) 563–578, https://doi.org/10.1016/j.energy.2017.09.100.

[13] P. Chen, C. Jia, C. Ng, Z. Hu, Application of SADA method on full-scale measurement data for dynamic responses prediction of Hywind floating wind turbines, Ocean Eng. 239 (Nov. 2021), 109814, https://doi.org/10.1016/J.OCEANENG.2021.109814.

[14] T.R. Lucas, A.F. Ferreira, R.B. Santos Pereira, M. Alves, Hydrogen production from the WindFloat Atlantic offshore wind farm: a techno-economic analysis, Appl. Energy 310 (Mar. 2022), 118481, https://doi.org/10.1016/J.APENERGY.2021.118481.

[15] M.T. Qaiser, J. Ejaz, O. Osen, A. Hasan, Digital twin-driven energy modeling of Hywind Tampen floating wind farm, Energy Rep. 9 (Oct. 2023) 284–289, https://doi.org/10.1016/J.EGYR.2023.09.023.

[16] D.S. Ochs, R.D. Miller, W.N. White, Simulation of electromechanical interactions of permanent-magnet direct-drive wind turbines using the fast aeroelastic simulator, IEEE Trans. Sustain. Energy 5 (1) (2014) 2–9, https://doi.org/10.1109/TSTE.2013.2269681.

[17] A. Honrubia-Escribano, E. Gómez-Lázaro, J. Fortmann, P. Sørensen, S. Martin-Martinez, Generic dynamic wind turbine models for power system stability analysis: a comprehensive review, Renew. Sustain. Energy Rev. 81 (January 2017) 1939–1952, https://doi.org/10.1016/j.rser.2017.06.005, 2018.

[18] O.N. Nobela, R.C. Bansal, J.J. Justo, A review of power quality compatibility of wind energy conversion systems with the South African utility grid, Renew. Energy Focus 31 (Dec. 2019) 63–72, https://doi.org/10.1016/J.REF.2019.10.001.

[19] B. Li, H. Zhao, S. Gao, S. Hu, Digital real-time co-simulation platform of refined wind energy conversion system, Int. J. Electr. Power Energy Syst. 117 (2020), 105676, https://doi.org/10.1016/j.ijepes.2019.105676. July 2019.

[20] B. Yang, T. Yu, H. Shu, J. Dong, L. Jiang, Robust sliding-mode control of wind energy conversion systems for optimal power extraction via nonlinear perturbation observers, Appl. Energy 210 (2018) 711–723, https://doi.org/10.1016/j.apenergy.2017.08.027. July 2017.

[21] A. Pratap, N. Urasaki, T. Senjyu, Instantaneous frequency and voltage control of PMSG-based WECS using controllable load, Proc. Int. Conf. Power Electron. Drive Syst. 6 (2013) 468–473, https://doi.org/10.1109/PEDS.2013.6527064.

[22] A. Akinrinde, A. Swanson, R. Tiako, Dynamic behavior of wind turbine generator configurations during ferroresonant conditions, Energies 12 (4) (2019) 1–16, https://doi.org/10.3390/en12040639.

[23] D. Zhang, K.J. Tseng, Design and Modelling of Grid-Connected PMSG-Based Wind Energy Conversion through Diode Rectifier, DC/DC and DC/AC Converters, 2014 Australas. Univ. Power Eng. Conf. AUPEC 2014 - Proc., 2014, pp. 1–5, https://doi.org/10.1109/AUPEC.2014.6966520. October.

[24] Y. Guo, X. Wang, Y. Mei, Z. Ye, X. Guo, Effect of coupled platform pitch-surge motions on the aerodynamic characters of a horizontal floating offshore wind turbine, Renew. Energy 196 (Aug. 2022) 278–297, https://doi.org/10.1016/J.RENENE.2022.06.108.

[25] B. Golparvar, P. Papadopoulos, A.A. Ezzat, R.Q. Wang, A surrogate-model-based approach for estimating the first and second-order moments of offshore wind power, Appl. Energy 299 (Oct. 2021), 117286, https://doi.org/10.1016/J.APENERGY.2021.117286.

[26] J. Carmona-Sanchez, Z. Lin, M. Collu, M. Barnes, O. Marjanovic, D. Cevasco, An analysis of the impact of an advanced aero-hydro-servo-elastic model of dynamics on the generator-converter dynamics, for an offshore fixed 5MW PMSG wind turbine, IET Conf. Publ. CP751 (2019) 1–6, https://doi.org/10.1049/cp.2019.0080, 2019.

[27] K.A. Shah, et al., A synthesis of feasible control methods for floating offshore wind turbine system dynamics, Renew. Sustain. Energy Rev. 151 (2021), https://doi.org/10.1016/j.rser.2021.111525. July.

[28] F. Meng, et al., Co-located offshore wind–wave energy systems: can motion suppression and reliable power generation be achieved simultaneously? Appl. Energy 331 (Feb. 2023), 120373 https://doi.org/10.1016/J.APENERGY.2022.120373.

[29] A. Cordle, J. Jonkman, State of the art in floating wind turbine design tools, Proc. Int. Offshore Polar Eng. Conf. (2011) 367–374. October.

[30] A. Beardsell, A. Alexandre, B. Child, R. Harries, D. McCowen, Beyond OC5 - further advances in floating wind turbine modelling using Bladed, J. Phys. Conf. Ser. 1102 (1) (2018), https://doi.org/10.1088/1742-6596/1102/1/012023.

[31] M.L.B. Jr, FAST User Guide 2005," *Contract*, 2005. October.

[32] Y. Xia, K.H. Ahmed, B.W. Williams, Wind turbine power coefficient analysis of a new maximum power point tracking technique, IEEE Trans. Ind. Electron. 60 (3) (2013) 1122–1132, https://doi.org/10.1109/TIE.2012.2206332.

[33] Q. Xing-hong, L. Yong, Y. Jun, L. Ren, Design of grid-connected converter for a permanent magnet synchronous direct-drive wind power generation System.pdf, Power Electron 42 (3) (2008) 22–34.

[34] J. Jonkman, S. Butterfield, W. Musial, G. Scott, Definition of a 5-MW Reference Wind Turbine for Offshore System Development, 2009, https://doi.org/10.1115/1.4038580.

[35] A.M. Hemeida, W. a Farag, O. a Mahgoub, Modeling and control of direct driven PMSG for ultra large wind turbines, Eng. Technol. 59 (2011) 918–924. August 2015.

[36] R.Y. Yang, C.W. Wang, C.C. Huang, C.H. Chung, C.P. Chen, C.J. Huang, The 1:20 scaled hydraulic model test and field experiment of barge-type floating offshore wind turbine system, Ocean Eng. 247 (Mar. 2022), 110486, https://doi.org/10.1016/J.OCEANENG.2021.110486.

[37] L. Chen, B. Basu, Wave-current interaction effects on structural responses of floating offshore wind turbines, Wind Energy 22 (2) (2019) 327–339, https://doi.org/10.1002/we.2288.

[38] J. Yang, Y.P. He, Y.S. Zhao, Y.L. Shao, Z.L. Han, Experimental and numerical studies on the low-frequency responses of a spar-type floating offshore wind turbine, Ocean Eng. 222 (2021), 108571, https://doi.org/10.1016/j.oceaneng.2021.108571. January.

[39] B.J. Jonkman, TurbSim User's Guide, 2009. September, Version 1.50.

[40] A.C.P.A.S. Committee, ACP 61400-1-202x: Wind Energy Generation Systems – Part 1: Design Requirements – Modified Adoption of IEC 61400-1, fourth ed., 2019. Washington DC.

[41] J.M. Jonkman, Dynamics Modeling and Loads Analysis of an Offshore Floating Wind Turbine 8 (11) (2007).

[42] D.J.T. Carter, Prediction of wave height and period for a constant wind velocity using the JONSWAP results, Ocean Eng. 9 (1) (Jan. 1982) 17–33, https://doi.org/10.1016/0029-8018(82)90042-7.

[43] R.L. Soulsby, Simplified calculation of wave orbital velocities, Report TR 155, p. 12, HR Wallingford Rep. TR 155 (2006) [Online], http://eprints.hrwallingford.co.uk/692/1/TR155.pdf.

[44] M. Cui, J. Zhang, A.R. Florita, B.M. Hodge, D. Ke, Y. Sun, An optimized swinging door algorithm for identifying wind ramping events, IEEE Trans. Sustain. Energy 7 (1) (2016) 150–162, https://doi.org/10.1109/TSTE.2015.2477244.

[45] R. Hemmati, H. Mehrjerdi, M. Shafie-Khah, P. Siano, J.P.S. Catalao, Managing multitype capacity resources for frequency regulation in unit commitment integrated with large wind ramping, IEEE Trans. Sustain. Energy 12 (1) (2021) 705–714, https://doi.org/10.1109/TSTE.2020.3017231.

[46] D. Lyners, H. Vermeulen, M. Groch, Wind power ramp event detection using a multi-parameter segmentation algorithm, Energy Rep. 7 (Nov. 2021) 5536–5548, https://doi.org/10.1016/J.EGYR.2021.08.137.

[47] T. Ackermann, Wind Power in Power Systems, 2005.

[48] J. Jonkman, W. Musial, Offshore Code Comparison Collaboration (OC3) for IEA Task 23 Offshore Wind Technology and Deployment Offshore Code Comparison Collaboration (OC3) for IEA Task 23 Offshore Wind Technology and Deployment, December, 2010, pp. 1–74 [Online]. Available: https://www.nrel.gov/docs/fy11osti/48191.pdf.

[49] M.J. Muliawan, M. Karimirad, Z. Gao, T. Moan, Extreme responses of a combined spar-type floating wind turbine and floating wave energy converter (STC) system with survival modes, Ocean Eng. 65 (2013) 71–82, https://doi.org/10.1016/j.oceaneng.2013.03.002.

[50] J.J. Yang, E.M. He, Coupled modeling and structural vibration control for floating offshore wind turbine, Renew. Energy 157 (2020) 678–694, https://doi.org/10.1016/j.renene.2020.05.075.

[51] S. Earle, Physical Geology, second ed., 2019.